

# Aerodynamic Characterization of a Microspoiler System for Supersonic Finned Projectiles

Edward Scheuermann\* and Mark Costello†

Georgia Institute of Technology, Atlanta, Georgia 30332-0150

and

Sidra Silton‡ and Jubaraj Sahu§

U.S. Army Research Laboratory, Aberdeen, Maryland 21005-5066

DOI: 10.2514/1.A33005

To create highly maneuverable projectiles, some physical control mechanism is needed that is capable of altering the projectile trajectory in a desired manner. The work reported here considers a small flow control device, termed a microspoiler system, located between the rear stabilizing fins of a projectile. Such a mechanism relies on the boundary-layer shock interaction between the projectile body, rear stabilizing fins, and microspoilers to provide a multiplicative effect on controllable forces and moments. To investigate performance of the microspoiler control mechanism, projectile trajectories with microspoilers were generated both computationally using a coupled CFD and rigid-body dynamic simulation and experimentally from spark range testing. Using this computational and experimental trajectory information, aerodynamic coefficients both with and without microspoilers were estimated and found to be in good agreement where the major effect of the microspoiler system is the addition of trim forces and moments along with a slight increase in axial forces. Additionally, control authority of a basic finned projectile equipped with an active microspoiler system is investigated for a typical direct-fire shooting scenario.

## Nomenclature

$C_{lp}$	=	roll damping aerodynamic coefficient
$C_{l\delta}$	=	roll moment aerodynamic coefficient from fin cant
$C_{mq}$	=	pitch damping moment aerodynamic coefficient
$C_{m\alpha}$	=	angle-of-attack-dependent pitching moment aerodynamic coefficient
$C_{m0}, C_{n0}$	=	trim moment aerodynamic coefficients, perpendicular to projectile axis of symmetry
$C_{N\alpha}$	=	angle-of-attack-dependent normal force aerodynamic coefficient
$C_{X0}$	=	zero angle-of-attack axial force aerodynamic coefficient, parallel to projectile axis of symmetry
$C_{X2}$	=	angle-of-attack-dependent axial force aerodynamic coefficient, parallel to projectile axis of symmetry
$C_{Y0}, C_{Z0}$	=	trim force aerodynamic coefficients, perpendicular to projectile axis of symmetry
$D$	=	projectile reference diameter, m
$g$	=	acceleration due to gravity, 9.81 m/s <sup>2</sup>
$I$	=	projectile inertia tensor matrix, kg·m <sup>2</sup>
$I_B, J_B, K_B$	=	projectile body reference frame axes along the $x$ , $y$ , and $z$ directions
$I_I, J_I, K_I$	=	inertial reference frame axes along the $x$ , $y$ , and $z$ directions
$L, M, N$	=	total external moment components exerted on the projectile body expressed in the projectile body reference frame, N·m
$m$	=	projectile mass, kg

$p, q, r$	=	components of the projectile angular velocity vector expressed in the projectile body reference frame, rad/s
$u, v, w$	=	components of the projectile mass center velocity vector expressed in the projectile body reference frame, m/s
$V$	=	total velocity magnitude of projectile mass center, m/s
$X, Y, Z$	=	total external force components exerted on the projectile body expressed in the projectile body reference frame, N
$x, y, z$	=	inertial position components of projectile mass center, m
$\delta$	=	fin cant angle, deg
$\rho$	=	atmospheric density, kg/m <sup>3</sup>
$\phi, \theta, \psi$	=	Euler roll, pitch, and yaw angles defining projectile orientation, deg

## I. Introduction

DESIGN and development of accurate guided projectiles presents weapons designers with numerous technical challenges. In particular, accurate determination of the projectile aerodynamics and the creation of precise yet cost-efficient control mechanisms are two highly popularized areas of research within the ballistics and smart weapons community. Such a control mechanism is essential to improving accuracy and reducing dispersion error over conventional rounds and must be capable of altering the projectile trajectory to correct for aiming errors due to variable atmospheric conditions, firing platform motion, or manufacturing inaccuracies of the gun tube, propellant, or the projectile itself. Furthermore, the physical control mechanism and associated electronics inherent to guided projectiles must be robust to withstand the extreme accelerations and spin rates experienced at launch and during flight, yet inexpensive to manufacture and deploy large quantities of such munitions at once.

In recent years, many different active control mechanisms for guided projectiles have been investigated, including moveable canards and other lifting surface appendages [1–3], deployable pins [4,5], gas jet or explosive thrusters [6–8], and translation or rotation of internal components [9]. Although each of these devices are capable of altering the projectile trajectory in some desired manner, this paper focuses on the microspoiler mechanism for high-speed

Received 26 March 2014; revision received 30 April 2014; accepted for publication 17 July 2014; published online 28 October 2014. Copyright © 2014 by the American Institute of Aeronautics and Astronautics, Inc. All rights reserved. Copies of this paper may be made for personal or internal use, on condition that the copier pay the \$10.00 per-copy fee to the Copyright Clearance Center, Inc., 222 Rosewood Drive, Danvers, MA 01923; include the code 1533-6794/14 and \$10.00 in correspondence with the CCC.

\*Graduate Research Assistant, Woodruff School of Mechanical Engineering, Student Member AIAA.

†Professor, Guggenheim School of Aerospace Engineering, Woodruff School of Mechanical Engineering, Associate Fellow AIAA.

‡Aerospace Engineer, Weapons and Materials Research Directorate, Associate Fellow AIAA.

§Aerospace Engineer, Weapons and Materials Research Directorate, Fellow AIAA.

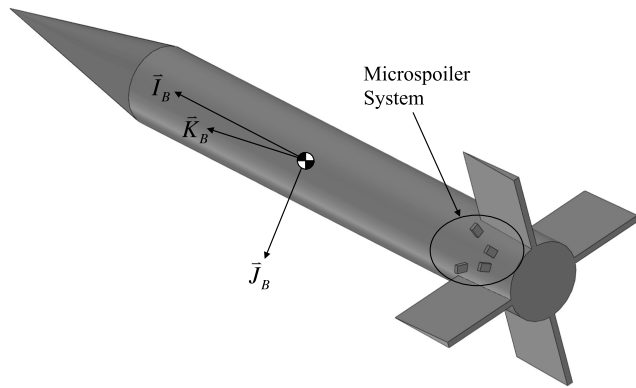


Fig. 1 Basic finned projectile with microspoiler mechanism.

finned projectiles previously investigated by Dykes et al. [10]. The microspoiler mechanism consists of an array of small protrusions, termed microspoilers, extending outward from the projectile body and located between the rear stabilizing fins. At supersonic speeds, the microspoiler mechanism induces an aerodynamic force and moment perturbation resulting from the interaction of the shock waves with the rear stabilizing fins, projectile body, and microspoilers. By actively extending and retracting the microspoiler array in concert with the projectile roll angle, the resulting aerodynamic perturbation can be used for control to precisely alter the projectile trajectory as needed. Several researchers have previously considered protuberance effects on fin-body interactions of supersonic projectiles [4,5,11,12], and both computational and experimental analysis have shown that significant force multiplication can exist by modifying the boundary-layer shock interaction of the projectile fin and body.

The work reported here investigates the aerodynamic perturbation effects of a small array of microspoilers inserted between the rear stabilizing fins of a basic finned projectile. Figure 1 illustrates a finned projectile equipped with a single microspoiler array. Using trajectory information obtained from computational analysis and experimental spark range testing, two different aerodynamic models were numerically estimated, representing projectile configurations both with and without microspoilers. Flight dynamic performance in terms of maximum control authority was also investigated for a simple left turn prototype maneuver and later presented as several parametric trade studies. The paper begins with a description of the computational and experimental trajectory generation techniques followed by a review of the nonlinear projectile dynamic model used for all aerodynamic coefficient estimation and control authority studies. Next, the aerodynamic coefficient estimation procedure and resulting coefficients using both the computational and experimental spark range trajectories are presented, followed by several parametric trade studies demonstrating the expected control authority of the active microspoiler control mechanism.

## II. Computational Trajectory Generation

The computational generation of projectile trajectories was achieved using a combined computational fluid dynamic and rigid-body dynamic simulation (CFD/RBD) algorithm. This method, also referred to as the virtual fly-out method, simulates free-flight projectile motion from first principles by numerically integrating the projectile dynamic model forward in time using the aerodynamic loads computed by CFD to drive projectile motion. In previous work, this CFD/RBD analysis technique has been shown to accurately predict ballistic trajectories for a wide range of fin-stabilized projectile configurations [13–16].

Using the basic Army–Navy finner (ANF) projectile as the testbed projectile for this study, two different configurations were analyzed at velocities of Mach 2.0, 2.5, and 3.0: a baseline (symmetric) configuration without microspoilers and a controlled (asymmetric) configuration with one array of fixed microspoilers. In this context, a single array of microspoilers refers to the entire group of four small

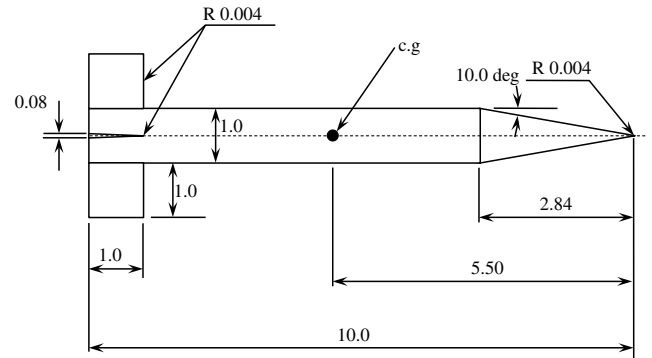


Fig. 2 ANF projectile schematic drawing.

planar protrusions extending outward from the projectile body located between two of the four rear stabilizing fins. Also, the distinction between active and fixed microspoiler arrays addresses the concept that a fixed array remains extended and fixed in place throughout the entire trajectory. Alternatively, an active microspoiler array may be extended or retracted in conjunction with the projectile roll angle such that the aerodynamic perturbation effects resulting from the extended microspoiler array are used for trajectory control. By comparing trajectories from the baseline and controlled projectile configurations, perturbation effects from a single microspoiler array are easily isolated and identified. Although the microspoiler mechanism is not exclusive to the ANF projectile, the ANF was selected given its commonplace within the academic community and well-documented aerodynamics. Figure 2 presents basic ANF projectile geometry normalized by the munition reference diameter (caliber). Table 1 details the actual ANF projectile parameters used within the CFD/RBD analysis.

The CFD analysis required different computational meshes for each projectile configuration. A structured multiblock mesh consisting of 12 million hexahedral cells was generated for the baseline configuration. To easily mesh the controlled configuration, additional structured blocks were created in the region containing the microspoilers resulting in an overall mesh of 14 million cells. Note most of the grid points were clustered near the boundary layer, rear stabilizing fins, microspoilers, and wake regions. Additional details of the computational meshes can be found in [16].

The projectile dynamic model associated with the RBD module consists of a nonlinear, six-degree-of-freedom (6-DOF) rigid-body dynamic model. The six degrees of freedom are composed of three inertial position components ( $x$ ,  $y$ , and  $z$ ) and three Euler orientation angles ( $\phi$ ,  $\theta$ , and  $\psi$ ) conforming to the standard aerospace (body-fixed, 3-2-1) rotation sequence. All aerodynamic forces and moments are computed from the CFD simulation and subsequently passed to the projectile dynamic model such that the governing equations of motion can be numerically integrated forward in time. In terms of the aerodynamic flow solution, the complete set of three-dimensional (3-D) time-dependent Navier–Stokes equations is solved in a time-accurate manner using the commercially available code CFD++. The 3-D, time-dependent, Reynolds-averaged Navier–Stokes (RANS) equations are solved using the following finite volume equation:

$$\frac{\partial}{\partial t} \int_V \mathbf{W} dV + \oint (\mathbf{F} - \mathbf{G}) dA = \int_V \mathbf{H} dV \quad (1)$$

Table 1 ANF projectile parameters used in CFD/RBD study

Description	Value
Reference diameter $D$ , mm	30.0
Mass center location $SL_{COP}$ , mm (measured from rear)	135.0
Mass $m$ , kg	1.588
Roll inertia $I_{XX}$ , kg-m <sup>2</sup>	$1.92526 \times 10^{-4}$
Pitch inertia $I_{YY}$ , kg-m <sup>2</sup>	$9.87035 \times 10^{-3}$
Fin cant angle $\delta$ , deg	0.0

where  $\mathbf{W}$  is the vector of conservative variables;  $\mathbf{F}$  and  $\mathbf{G}$  are the inviscid and viscous flux vectors, respectively;  $\mathbf{H}$  is the vector of source terms;  $V$  is the cell volume; and  $A$  is the surface area of the cell face. A higher-order, two-equation RANS turbulence model was used for the computation of the turbulent flows that are of interest. Equations (2) and (3) show the commonly used  $k$ - $\epsilon$  model [17] employed here:

$$\frac{d(\rho k)}{dt} = \nabla \left[ \left( \mu + \frac{\mu_t}{\sigma_k} \right) \nabla k \right] + P_k - \rho \epsilon \quad (2)$$

$$\frac{d(\rho \epsilon)}{dt} = \nabla \left[ \left( \mu + \frac{\mu_t}{\sigma_\epsilon} \right) \nabla \epsilon \right] + (C_{\epsilon 1} P_k - C_{\epsilon 2} \rho \epsilon + E) T_l^{-1} \quad (3)$$

Note that  $k$  represents the turbulence kinetic energy,  $\epsilon$  is the turbulence dissipation rate, and  $\mu_t$  is the turbulence eddy viscosity, which is a function of both  $k$  and  $\epsilon$ . Additionally,  $P_k$  is a production term,  $E$  is a source term, and  $T_l$  is a realizable time scale. This turbulence model has been successfully and routinely used in a number of projectile and other aerodynamics applications. These turbulence equations are fully solved to the wall of the projectile and require high-resolution meshes near the projectile surface.

In the virtual fly-out computations, a dual time-stepping technique was used to achieve the desired time-accurate solution. The first time step corresponds to the time discretization of the physical time variation term. This time step is typically set to a value representing approximately 1/100th of the period of oscillation expected in the transient flow. The second time step (i.e., inner time step) is an artificial time variation term added to the basic physical transient equations. For the inner iterations, the time step is allowed to vary spatially and is selected to help satisfy the physical transient equations to the desired degree. Often, several internal iterations (10–20) are required, depending on the magnitude of the outer time step, the nature of the problem and boundary conditions, and the consistency of the mesh with respect to the physics at hand. In the present work, an outer time step of  $1.745 \times 10^{-4}$  s and 10 inner iterations were used for all virtual fly-out simulations. Solution convergence was monitored via reduction of residuals of the RANS equations, as well as the time history of relevant aerodynamic forces and moments. Several orders of magnitude reduction in the global residuals and at least one order of magnitude reduction in inner time step residuals were required. Grid convergence studies have also been performed in previous work [18,19] where similar meshes were used to predict aerodynamic forces and moments that were in excellent agreement with the experimental data. As a result, the computational grid used here is thus deemed sufficient to produce the desired accuracy of forces and moments for the same projectile geometry.

### III. Experimental Trajectory Generation

Projectile trajectories both with and without microspoilers were obtained experimentally at Aberdeen Proving Ground, Maryland. During such tests, a prototype projectile was fired along a flat trajectory through an enclosed building. At discrete points along its ballistic flight path, a series of orthogonal spark photography stations (i.e., horizontal and vertical planes) were used to capture a snapshot of the projectile position and orientation. Figure 3 provides an example spark shadowgraph of a finned projectile in supersonic flight.

In an effort to replicate the computational trajectory generation procedure described in Sec. II, two different projectile configurations were designed and test fired within the spark range: a baseline (symmetric) projectile without microspoilers and a controlled (asymmetric) projectile with one array of fixed microspoilers. Launch velocities of Mach 2.0, 2.5, and 3.0 were selected, with several shots of each projectile configuration at each speed to ensure repeatability. The details of the spark range test matrix are provided in Table 2. Again, the testbed projectile for all spark range testing was the basic ANF. Given the strict size constraints of the gun tube and test range itself, projectile size, mass, and fin cant angle were

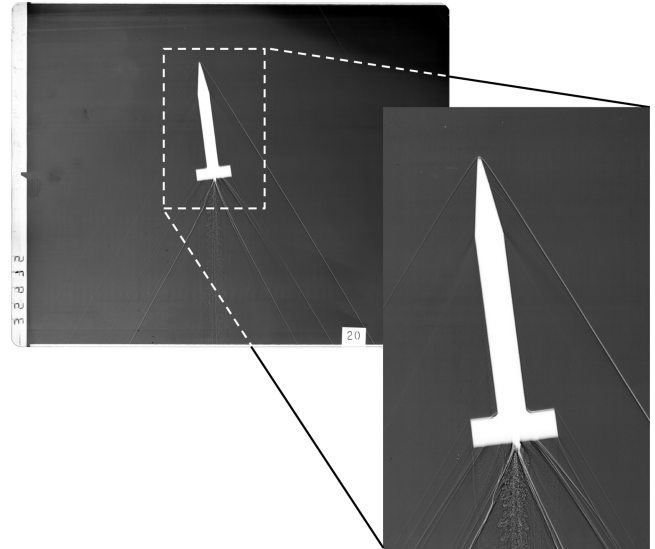


Fig. 3 Spark shadowgraph of ANF projectile in supersonic flight.

appropriately sized to generate sufficient motion and ensure accurate estimation of the aerodynamic coefficients associated with microspoiler deployment while keeping the projectile within the field of view of the spark range cameras (28 × 36 cm) throughout the entire length of the range (~100 m). The final design parameters for the spark range test projectile are listed in Table 3.

For ease of manufacturing, the entire test projectile was machined directly from 25-mm-diam 7075 aluminum using all computer controlled machinery. Total projectile weight was 10.7 g, with its mass center located at approximately 40% of the overall projectile length measured from the rear. Note this mass-center location was slightly aft of the nominal mass-center location of 45% for the ANF; however, the resulting decrease in static margin was not significant to adversely affect the flight performance of the projectile and was thus deemed acceptable. To limit the projectile roll rate during flight, a 25 mm smooth bore gun tube was selected in combination with 1 deg of fin cant to initiate roll-up immediately following launch. Maximum tip-to-tip fin span was 24.23 mm, leaving a small amount of radial clearance within the selected gun tube. Additionally, a stacked microspoiler insert for the controlled configuration, shown in Fig. 4, was designed to precisely replicate the microspoiler geometry. The final manufactured test projectile and sabot system can be seen in Fig. 5. In total, 36 shots were recorded on film: 14 baseline (symmetric) rounds and 22 controlled (asymmetric) rounds. On

Table 2 Spark range test quantities and target velocities

Mach no.	Velocity, m/s	Quantity fired	Configuration
2.00	680	2–3	Baseline
		3–5	Controlled
2.50	850	2–3	Baseline
		3–5	Controlled
3.00	1026	2–3	Baseline
		3–5	Controlled

Table 3 Final spark range test projectile configuration

Description	Value
Reference diameter $D$ , mm	8.08
Mass center location $SL_{COP}$ , mm (Measured from rear)	31.83
Mass $m$ , gram	10.7
Roll inertia $I_{XX}$ , kg·m <sup>2</sup>	$1.43974 \times 10^{-7}$
Pitch inertia $I_{YY}$ , kg·m <sup>2</sup>	$4.92367 \times 10^{-6}$
Fin cant angle $\delta$ , deg	1.0

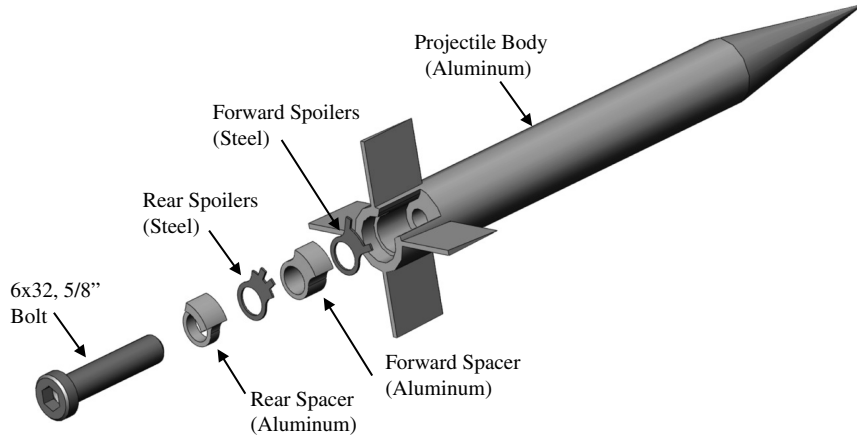


Fig. 4 Exploded view of controlled projectile aftbody assembly.



Fig. 5 Prototype projectile and sabot components.

average, each successful shot was composed of between 15–40 measured data points.

#### IV. Projectile Dynamic Model

Before proceeding further, a description of the projectile dynamic model used in later sections for both aerodynamic coefficient estimation and control authority determination is provided as reference for the reader. The projectile dynamic model used in the present work is a standard 6-DOF nonlinear rigid-body model typically employed in projectile flight dynamic modeling. The six degrees of freedom include three inertial components of the projectile mass-center position, denoted  $x$ ,  $y$ , and  $z$ , and three Euler orientation angles, denoted  $\phi$ ,  $\theta$ , and  $\psi$ . The equations of motion as described in [20,21] are provided in Eqs. (4–7):

$$\begin{Bmatrix} \dot{x} \\ \dot{y} \\ \dot{z} \end{Bmatrix} = \begin{bmatrix} c_\theta c_\psi & s_\phi s_\theta c_\psi - c_\phi s_\psi & c_\phi s_\theta c_\psi + s_\phi s_\psi \\ c_\theta s_\psi & s_\phi s_\theta s_\psi + c_\phi c_\psi & c_\phi s_\theta s_\psi - s_\phi c_\psi \\ -s_\theta & s_\phi c_\theta & c_\phi c_\theta \end{bmatrix} \begin{Bmatrix} u \\ v \\ w \end{Bmatrix} \quad (4)$$

$$\begin{Bmatrix} \dot{\phi} \\ \dot{\theta} \\ \dot{\psi} \end{Bmatrix} = \begin{bmatrix} 1 & s_\phi t_\theta & c_\phi t_\theta \\ 0 & c_\phi & -s_\theta \\ 0 & s_\phi/c_\theta & c_\phi/c_\theta \end{bmatrix} \begin{Bmatrix} p \\ q \\ r \end{Bmatrix} \quad (5)$$

$$\begin{Bmatrix} \dot{u} \\ \dot{v} \\ \dot{w} \end{Bmatrix} = \begin{Bmatrix} X/m \\ Y/m \\ Z/m \end{Bmatrix} - \begin{bmatrix} 0 & -r & q \\ r & 0 & -p \\ -q & p & 0 \end{bmatrix} \begin{Bmatrix} u \\ v \\ w \end{Bmatrix} \quad (6)$$

$$\begin{Bmatrix} \dot{p} \\ \dot{q} \\ \dot{r} \end{Bmatrix} = [I]^{-1} \left[ \begin{Bmatrix} L \\ M \\ N \end{Bmatrix} - \begin{bmatrix} 0 & -r & q \\ r & 0 & -p \\ -q & p & 0 \end{bmatrix} [I] \begin{Bmatrix} p \\ q \\ r \end{Bmatrix} \right] \quad (7)$$

where  $u$ ,  $v$ , and  $w$  represent the body frame components of the projectile mass center translational velocity, and  $p$ ,  $q$ , and  $r$  are the projectile angular velocity components expressed in the body frame. A simple flat-Earth inertial reference frame was employed for all simulations. Note the use of shorthand notation for trigonometric functions in Eqs. (4) and (5):  $s_\alpha \equiv \sin \alpha$ ,  $c_\alpha \equiv \cos \alpha$ , and  $t_\alpha \equiv \tan \alpha$ .

The total force terms  $X$ ,  $Y$ , and  $Z$ , appearing in Eq. (6) are composed of weight, aerodynamic, and microspoiler forces denoted with subscripts  $W$ ,  $A$ , and  $MS$ , respectively, as shown in Eq. (8):

$$\begin{Bmatrix} X \\ Y \\ Z \end{Bmatrix} = \begin{Bmatrix} X_W \\ Y_W \\ Z_W \end{Bmatrix} + \begin{Bmatrix} X_A \\ Y_A \\ Z_A \end{Bmatrix} + \begin{Bmatrix} X_{MS} \\ Y_{MS} \\ Z_{MS} \end{Bmatrix} \quad (8)$$

Note, all force and moment terms are expressed using body frame coordinates. Equation (9) details the body frame components of the weight force acting at the projectile mass center, where  $m$  is the projectile mass and  $g$  is the acceleration due to gravity:

$$\begin{Bmatrix} X_W \\ Y_W \\ Z_W \end{Bmatrix} = mg \begin{Bmatrix} -s_\theta \\ s_\phi c_\theta \\ c_\phi c_\theta \end{Bmatrix} \quad (9)$$

Similarly, the aerodynamic force components acting at the projectile center of pressure (COP) are shown in Eq. (10).

$$\begin{Bmatrix} X_A \\ Y_A \\ Z_A \end{Bmatrix} = -\frac{\pi}{8} \rho V^2 D^2 \begin{Bmatrix} C_{X0} + C_{X2}(v^2 + w^2)/V^2 \\ C_{N\alpha} v/V \\ C_{N\alpha} w/V \end{Bmatrix} \quad (10)$$

Note that  $\rho$  represents the atmospheric density,  $V$  is the total projectile velocity,  $D$  is the projectile reference diameter, and the quantities  $v/V$  and  $w/V$  approximate the projectile sideslip angle and aerodynamic angle of attack, respectively.

The asymmetric forces resulting from the microspoilers are shown in Eq. (11) and are simply modeled as two trim forces acting at the projectile mass center along the  $\mathbf{J}_B$  and  $\mathbf{K}_B$  axes:

$$\begin{Bmatrix} X_{MS} \\ Y_{MS} \\ Z_{MS} \end{Bmatrix} = -\frac{\pi}{8}\rho V^2 D^2 \begin{Bmatrix} 0 \\ C_{Y0} \\ C_{Z0} \end{Bmatrix} \quad (11)$$

The applied moments about the projectile mass center  $L$ ,  $M$ , and  $N$ , appearing in Eq. (7), are composed of steady aerodynamic, unsteady aerodynamic, and microspoiler moments denoted with subscripts  $S$ ,  $U$ , and  $MS$ , respectively, as shown in Eq. (12):

$$\begin{Bmatrix} L \\ M \\ N \end{Bmatrix} = \begin{Bmatrix} L_S \\ M_S \\ N_S \end{Bmatrix} + \begin{Bmatrix} L_U \\ M_U \\ N_U \end{Bmatrix} + \begin{Bmatrix} L_{MS} \\ M_{MS} \\ N_{MS} \end{Bmatrix} \quad (12)$$

The steady aerodynamic moments are simply computed as a cross product between the distance vector extending from the projectile mass center to the COP and the aerodynamic force components  $X_A$ ,  $Y_A$ , and  $Z_A$  as shown in Eq. (13):

$$\begin{Bmatrix} L_S \\ M_S \\ N_S \end{Bmatrix} = \begin{bmatrix} 0 & -\Delta WL_{COP} & \Delta BL_{COP} \\ \Delta WL_{COP} & 0 & -\Delta SL_{COP} \\ -\Delta BL_{COP} & \Delta SL_{COP} & 0 \end{bmatrix} \begin{Bmatrix} X_A \\ Y_A \\ Z_A \end{Bmatrix} \quad (13)$$

The terms  $\Delta SL_{COP}$ ,  $\Delta BL_{COP}$ , and  $\Delta WL_{COP}$  represent three components of the position vector from the projectile mass center to the COP along the  $I_B$ ,  $J_B$ , and  $K_B$  axes, respectively. Note that  $\Delta BL_{COP}$  and  $\Delta WL_{COP}$  are often zero, indicating an axisymmetric COP location. Although not explicitly shown in Eq. (13), an additional aerodynamic moment coefficient  $C_{m\alpha}$  is often used in modeling the steady aerodynamic moments. Equation (14) shows the relationship between  $C_{m\alpha}$ ,  $C_{N\alpha}$ , and  $\Delta SL_{COP}$  for an axisymmetric projectile:

$$C_{m\alpha} = \frac{1}{D} C_{N\alpha} \Delta SL_{COP} \quad (14)$$

The unsteady aerodynamic moments provide a damping source for the projectile angular motion as given by Eq. (15), where  $\delta$  represents the angle at which the rear stabilizing fins of the projectile are canted to induce roll during flight.

$$\begin{Bmatrix} L_U \\ M_U \\ N_U \end{Bmatrix} = \frac{\pi}{8}\rho V^2 D^3 \begin{Bmatrix} C_{l\delta}\delta + DC_{lp}p/2V \\ DC_{mq}q/2V \\ DC_{mq}r/2V \end{Bmatrix} \quad (15)$$

Lastly, the asymmetric moments resulting from the microspoilers are also modeled at two trim moments acting about the  $J_B$  and  $K_B$  axes, as shown in Eq. (16):

$$\begin{Bmatrix} L_{MS} \\ M_{MS} \\ N_{MS} \end{Bmatrix} = \frac{\pi}{8}\rho V^2 D^3 \begin{Bmatrix} 0 \\ C_{m0} \\ C_{n0} \end{Bmatrix} \quad (16)$$

Projectile mass, mass-center location, and inertial properties are all assumed to be constant throughout the entire flight duration. The location of the projectile COP and all aerodynamic coefficients depend on local Mach number and are linearly interpolated during simulation from a known aerodynamic data set. The dynamic system described by Eqs. (4–7) is numerically integrated forward in time from some known initial state using a fourth-order fixed time step Runge–Kutta algorithm.

## V. Aerodynamic Coefficient Estimation

Given the computationally generated and experimentally measured trajectories for each projectile configuration, the corresponding aerodynamic coefficients were estimated using a two-stage numerical optimization technique. This estimation technique, based largely on the Projectile Aerodynamic Coefficient Estimation

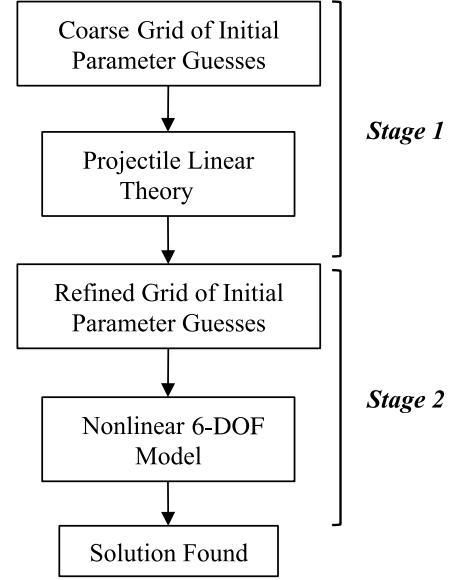


Fig. 6 Flowchart of two-stage numerical optimization technique.

(PACE) software tool (developed by Montalvo and Costello [22]) attempts to minimize the sum of the squared residuals between the generated trajectories and those simulated using a rigid-body dynamic model of the projectile where the unknown aerodynamic coefficients are treated as fitting parameters. Figure 6 provides a simple schematic depiction of the two-stage numerical optimization technique.

As with most optimization problems, the existence of local minima often complicate the process of converging upon the global optimum solution. To help eliminate local minimum errors, a coarse grid of initial starting values for the unknown parameters (i.e., aerodynamic coefficients) was first created and sent through a Levenberg–Marquardt numerical optimizer coupled with the rapid trajectory capability of projectile linear theory [23,24]. Next, a refined grid of initial conditions was created based on the previously optimized coefficients and was subsequently sent through a second output-error numerical optimizer combined with the nonlinear 6-DOF projectile model presented in Sec. IV to further minimize any residual between the generated and simulated trajectories. The final converged set of aerodynamic coefficients resulting from the second optimization state was considered to be the optimum solution.

## VI. Results

The following sections detail the aerodynamic coefficient fitting results using both computational and experimental trajectories. In the interest of brevity, trajectories from only one controlled projectile fit for each trajectory generation technique are presented. Lastly, a brief control authority trade study was performed to investigate the performance of the active microspoiler mechanism using both computationally and experimentally estimated aerodynamic models.

### A. Aerodynamic Coefficient Computation

For the computational technique, two different trajectories were generated at each target launch velocity of Mach 2.0, 2.5, and 3.0 [i.e., one baseline (symmetric) projectile and one controlled (asymmetric) projectile possessing one fixed microspoiler array]. Nominal initial conditions for each CFD/RBD simulation were  $x = 0$ ,  $y = 0$ , and  $z = 0$  m;  $\phi = 0$ ,  $\theta = 0$ , and  $\psi = 0$  rad;  $u = \text{Mach } 2.0, 2.5, \text{ and } 3.0$ ;  $v = 0$  and  $w = 0$  m/s; and  $p = 50$ ,  $q = 10$ , and  $r = 0$  rad/s. Note, to properly estimate the projectile roll damping coefficient, a small initial roll rate of 50 rad/s was provided. Also, an initial pitch rate of 10 rad/s was included to simulate the effects of muzzle launch disturbance during launch and to ensure sufficient cyclical excitation during flight. Using the time-accurate trajectory information

from the CFD/RBD simulation, the aerodynamic coefficients were estimated for both projectile configurations at each target launch velocity.

Figures 7–12 illustrate the controlled projectile trajectories from the CFD/RBD simulation and the projectile dynamic model presented in Sec. IV using the final estimated aerodynamic coefficients. Launch velocity was set to Mach 3.0. In each case, the estimated aerodynamic model agrees favorably with the CFD/RBD

simulation noting coefficients of determination near 80% and higher. Figures 7–9 present time histories of the translational kinematic states  $x$ ,  $y$ , and  $z$ . Note that, in Fig. 8, total lateral displacement  $y$  of the projectile reaches a maximum at approximately 3 m after 0.4 s of flight. The relatively large lateral displacement is primarily due to the nearly constant orientation of the microspoiler array within the lateral direction and subsequent control forces acting in the lateral direction following the decay in spin to nearly zero after 0.2 s of flight.

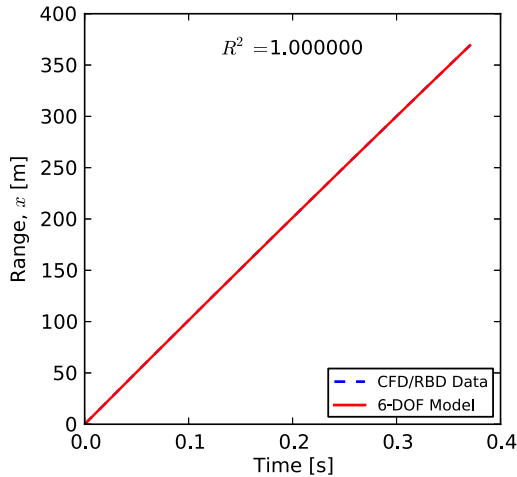


Fig. 7 CFD/RBD trajectory fit, range vs. time.

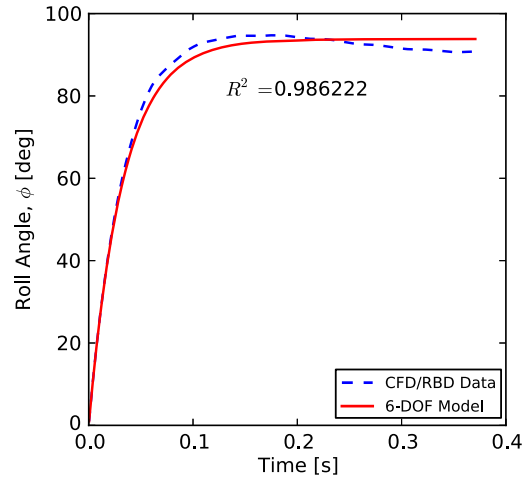


Fig. 10 CFD/RBD trajectory fit, roll angle vs. time.

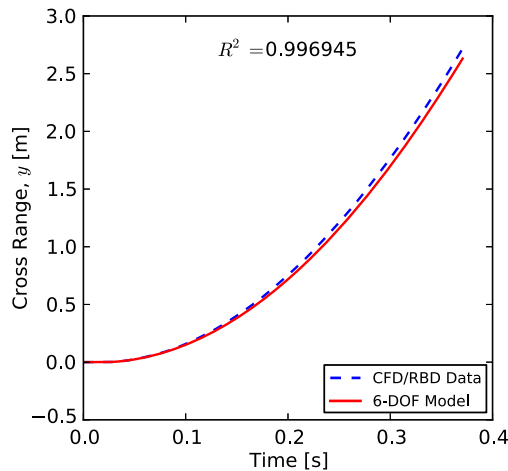


Fig. 8 CFB/RBD trajectory fit, cross range vs. time.

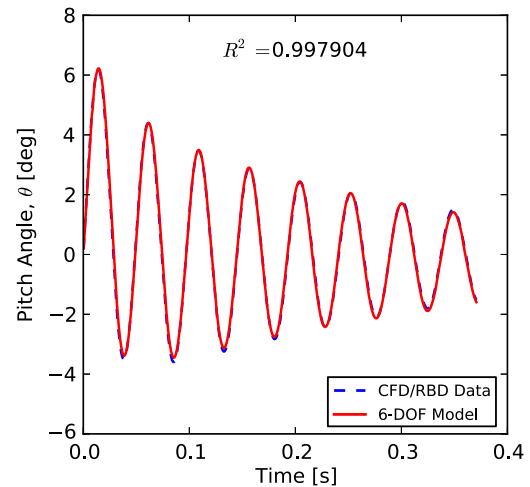


Fig. 11 CFD/RBD trajectory fit, pitch angle vs. time.

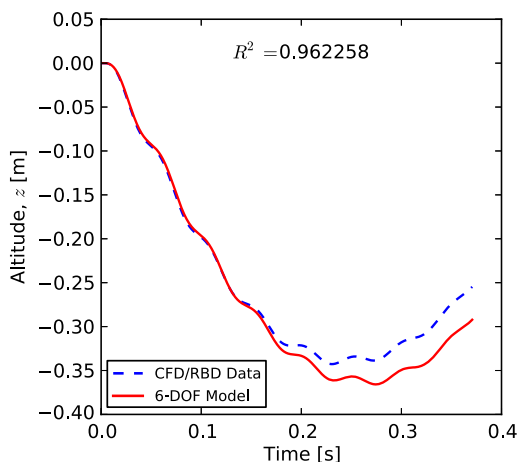


Fig. 9 CFD/RBD trajectory fit, altitude vs. time.

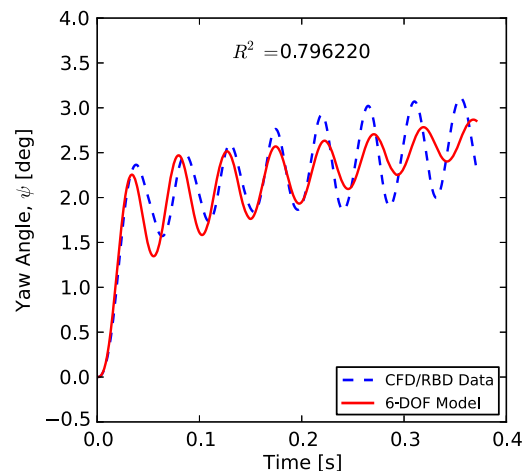


Fig. 12 CFD/RBD trajectory fit, yaw angle vs. time.

Figures 10–12 show the rotational kinematic states  $\phi$ ,  $\theta$ , and  $\psi$ . Considering the small initial roll rate and the fact that the rear stabilizing fins are not canted to induce roll during flight, a relatively small total roll displacement of approximately 90 deg is achieved as shown in Fig. 10. This small roll displacement was intended to prevent the projectile from being excessively stable and rolling too quickly, thus minimizing all asymmetric effects associated with the microspoiler array. Lastly, Figs. 11 and 12 show the projectile pitch and yaw angle time histories. Model agreement for pitch angle  $\theta$  is nearly exact, whereas some discrepancy exists for the projectile yaw angle  $\psi$ . Although the source of this error can largely be attributed to model uncertainty, the maximum error between the CFD/RBD simulation and the estimated aerodynamic model fit is less than 1.0 deg and was thus deemed acceptable.

In contrast to the computational technique, two additional factors must be considered when computing the aerodynamic coefficients from spark range test data. First, the only measured quantities for each spark range trajectory include the position and orientation of the projectile body at discrete, unequally spaced points along the length of the range. This is significantly different from the CFD/RBD trajectory information where all 12 states and the 6 forces and moments acting at the projectile mass center are explicitly calculated at each time step during the simulation. Assuming the first measurement point in the spark range data represents the initial projectile state, only half of the 12 required initial conditions are explicitly known. Consequently, the remaining six initial states (i.e.,  $u$ ,  $v$ ,  $w$ ,  $p$ ,  $q$ , and  $r$ ) must also be estimated in addition to the unknown aerodynamic coefficients to properly integrate the dynamic model forward in time. Second, the controlled projectile trajectories include the aerodynamic perturbation effects resulting from the fixed microspoiler array causing both an asymmetric force and moment, denoted  $\vec{F}_{MS}$  and  $\vec{M}_{MS}$ , respectively, on the projectile body during flight. Accordingly, proper orientation of the projectile body axes relative to the microspoiler array isolates the aerodynamic perturbation such that only two asymmetric trim coefficients ( $C_{Z0}$  and  $C_{m0}$ ) are needed to properly characterize the effect. Note that it was assumed that these two coefficients would largely capture the aerodynamic perturbation resulting from the microspoiler array, although minor changes in all coefficients are evident and are discussed in the following section. Figure 13 provides a rear view illustration of the controlled projectile with indicated body axes and microspoiler force and moment vectors. Considering that all aerodynamic loads exerted on the projectile are computed as components expressed within the projectile body reference frame, precise roll angle estimation is critical to properly resolving the resulting microspoiler forces and moments. Any residual or error between the measured and simulated projectile roll angle will corrupt the estimation process. To solve this problem, a proportional-derivative roll angle controller was implemented such that a small, nonphysical roll moment was applied to the projectile during flight, thus forcing the simulated roll angle to precisely match the measured

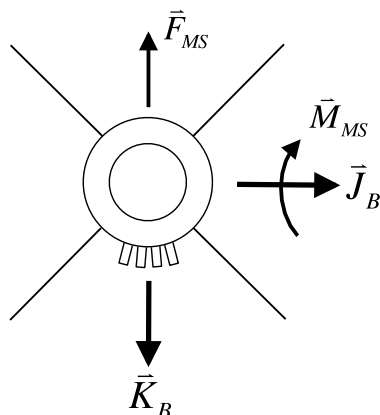


Fig. 13 Microspoiler forces and moments.

trajectory. This roll control moment was not needed for the CFD/RBD trajectories due to the low spin rate and low total roll displacement over the entire trajectory; however, each spark range trajectory required much higher spin rates with roll angle displacements in excess of 5000 deg such that the asymmetric microspoiler perturbation would not force the projectile outside of the spark photography viewing window during flight. Also, the magnitude of the applied moment was sufficiently small such that the overall ballistic trajectory of the projectile was not adversely affected.

Figures 14–19 compare the measured and simulated trajectories for an example controlled configuration spark range test firing. Launch velocity was calculated to be Mach 2.874 with a total of 21 measured data points. Model agreement for the translational kinematic states and the projectile roll angle shown in Figs. 14–17 was exceptionally accurate with calculated coefficients of determination above 99%. Note that the measured and simulated projectile roll angle in Fig. 17 are nearly exact, indicating proper resolution of the microspoiler forces and moments. Additionally, the measured and simulated Euler pitch and yaw angle time histories are shown in Figs. 18 and 19, with calculated coefficients of determination of 98.5 and 99.1%, respectively. Some model agreement degradation near the end of the measured trajectory was evident and can largely be attributed to modeling or measurement errors and manufacturing asymmetries of the projectile itself. Nevertheless, the overall model agreement for this particular shot was considered excellent and typical for the majority of all other spark range test firings.

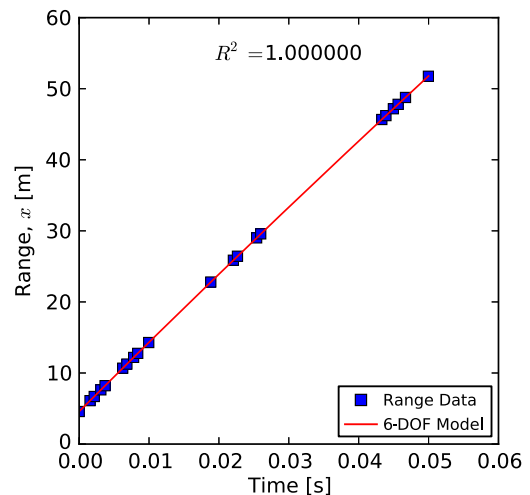


Fig. 14 Spark range trajectory fit, range vs time.

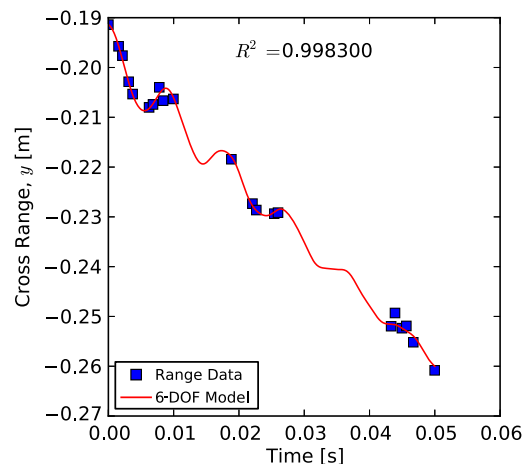


Fig. 15 Spark range trajectory fit, cross range vs time.

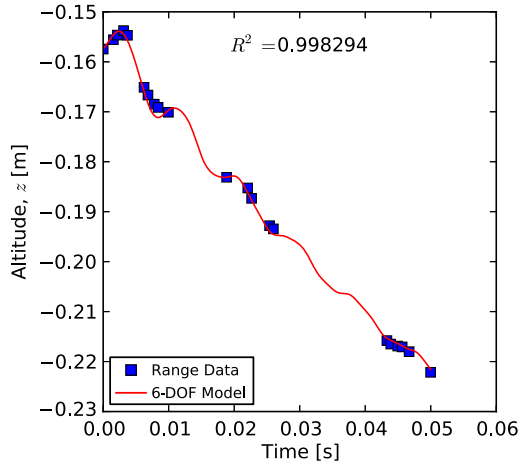


Fig. 16 Spark range trajectory fit, altitude vs time.

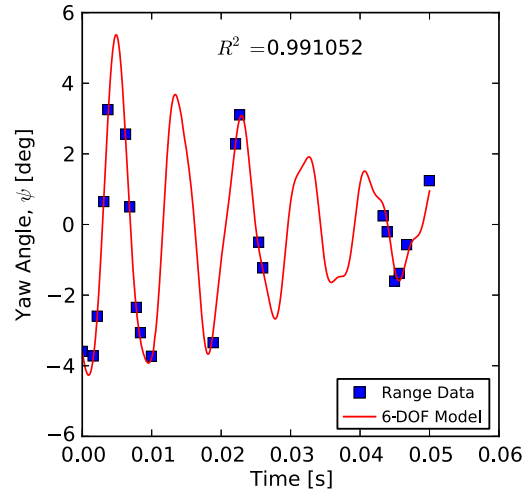


Fig. 19 Spark range trajectory fit, yaw angle vs time.

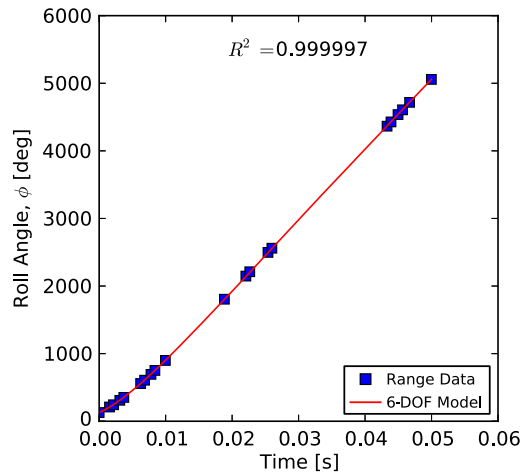


Fig. 17 Spark range trajectory fit, roll angle vs time.

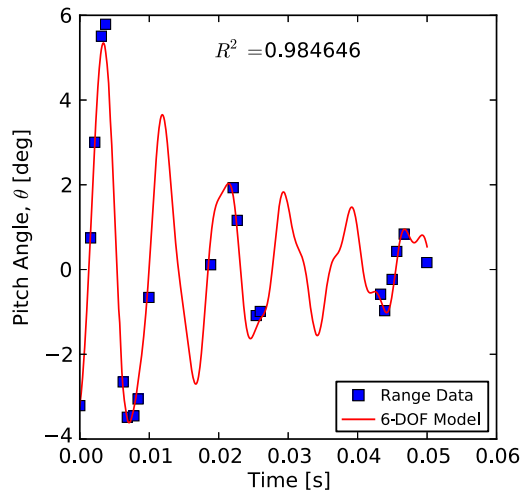


Fig. 18 Spark range trajectory fit, pitch angle vs time.

## B. Aerodynamic Coefficient Summary

Two different aerodynamic models were constructed for each coefficient as a function of Mach number. Each aerodynamic model corresponds to the baseline (symmetric) and controlled (asymmetric) projectile configurations. For comparison, the estimated aerodynamic coefficients from both computationally and experimentally generated trajectories at velocities of Mach 2.0, 2.5, and 3.0 are presented in

Table 4 where each coefficient entry lists the baseline (symmetric) value first followed by the controlled (asymmetric) value. Note that the aerodynamic coefficients estimated using the spark range data were interpolated from the entire data set and are presented at the desired Mach number. Also, all moment coefficients estimated from the spark range data were corrected to include the mass center at the nominal location of 45% of the overall projectile length measured from the rear to be consistent with the CFD/RBD data.

In total, seven different aerodynamic coefficients were estimated, including  $C_{X0}$ ,  $C_{lp}$ ,  $C_{N\alpha}$ ,  $C_{ma}$ ,  $C_{mq}$ ,  $C_{m0}$ , and  $C_{Z0}$ . Although the absolute values for some coefficients may vary between the CFD/RBD and spark range data, the basic trend between the baseline and controlled configurations are generally in good agreement. As expected, the base drag or axial force coefficient  $C_{X0}$  was higher by approximately 10% for the controlled configuration given the additional frontal area created by the microspoiler array. Pitch damping  $C_{mq}$  was also shown to increase slightly for the controlled configuration using the CFD/RBD data; however, it was shown to slightly decrease at Mach 2.0 for the spark range data and remain nearly unchanged at higher velocities. Similarly, the estimated value for roll damping  $C_{lp}$  using the CFD/RBD data increased slightly between the baseline and controlled configuration, whereas the spark range data indicated  $C_{lp}$  was slightly decreased at Mach 2.0 and nearly unchanged with increasing velocity. Although it was generally assumed that aerodynamic damping would increase for the asymmetric case given the disruption of the flow near the rear stabilizing fins caused by the microspoiler array, this apparent decrease in roll damping evident in the spark range data may be the result of manufacturing errors or uncertainty in the roll production coefficient  $C_{l\delta}$  with changing Mach number. Note that the influence of  $C_{l\delta}$  was not apparent in the CFD/RBD trajectories because the projectile model did not include fin cant.

The trim coefficients  $C_{Z0}$  and  $C_{m0}$  correspond to the microspoiler asymmetric perturbation force and moment, respectively. For each coefficient, values corresponding to the baseline configuration were fixed at zero, indicating a purely symmetric projectile. Small and consistent changes in  $C_{Z0}$  and  $C_{m0}$  were evident in both the CFD/RBD and spark range data at speeds of Mach 2.5 and higher. However, the estimated moment coefficient at Mach 2.0 using the spark range data is considerably less than that estimated from the CFD/RBD data. Similarly, the trim force coefficient  $C_{Z0}$  matches quite well between both estimated aerodynamic models, except at Mach 3.0 where the spark range estimate is significantly lower than that derived from the CFD/RBD data.

## C. Control Authority Characteristics

To evaluate the control authority of the microspoiler mechanism, a simple prototype maneuver was performed in which the projectile

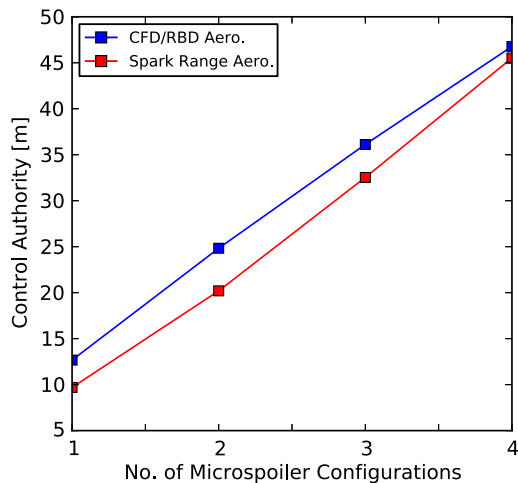
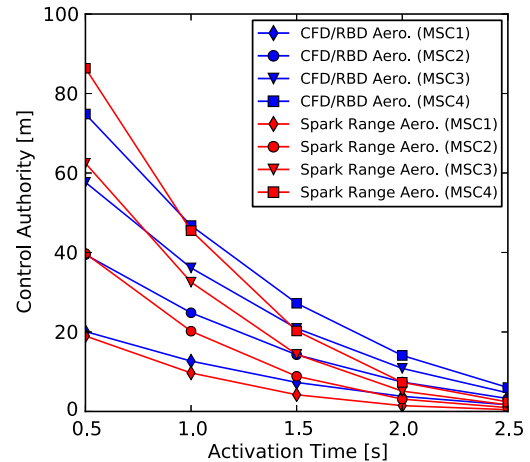
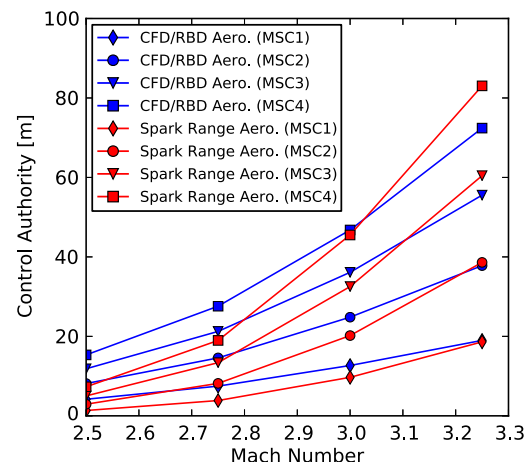
**Table 4** Estimated aerodynamic coefficient summary

Mach No.	CFD/RBD data			Spark range data		
	2.0	2.5	3.0	2.0	2.5	3.0
$C_{X0}$	0.54, 0.60	0.45, 0.50	0.39, 0.44	0.60, 0.66	0.52, 0.54	0.43, 0.46
$C_{lp}$	-27.76, -31.86	-23.35, -27.69	-20.21, -29.89	-28.53, -26.35	-21.57, -21.85	-17.57, -17.34
$C_{Na}$	10.80, 10.83	9.30, 9.42	8.45, 8.59	9.50, 11.42	9.21, 11.09	9.54, 10.71
$C_{ma}$	-24.04, -24.62	-16.95, -17.66	-12.91, -13.27	-21.55, -24.44	-14.94, -17.98	-12.67, -14.96
$C_{mq}$	-190.0, -236.4	-183.8, -256.4	-151.8, -214.5	-342.4, -299.0	-261.2, -259.5	-193.6, -214.2
$C_{m0}$	0.0, -0.64	0.0, -0.54	0.0, -0.42	0.0, -0.50	0.0, -0.56	0.0, -0.42
$C_{Z0}$	0.0, 0.19	0.0, 0.16	0.0, 0.11	0.0, 0.18	0.0, 0.13	0.0, 0.04

was commanded to make an abrupt left turn. Using the estimated aerodynamic coefficients computed from both the CFD/RBD virtual fly-out analysis and the spark range test firing, a more accurate depiction of the actual flight characteristics and overall performance of the microspoiler mechanism was achieved. Furthermore, the similarity in performance using aerodynamic data estimated both computationally and experimentally provides great insight as to the accuracy and effectiveness of the computational trajectory generation technique. To execute an inertial frame turning maneuver, a simple flight control system was implemented to actively switch the aerodynamic coefficients during flight between the baseline and controlled aerodynamic models, thus simulating the extension and retraction of the entire microspoiler array. Based on the measured projectile roll angle, the microspoiler array is first activated and later deactivated as the roll angle enters and exits the specified activation window, resulting in a constant aerodynamic perturbation or turning force applied to the projectile relative to the inertial reference frame. For simplicity, the switching of aerodynamic coefficients was modeled as a discrete change and does not include any actuator dynamics. Additionally, the flight control system was configured to model up to four independent microspoiler array sets located between each of the four rear stabilizing fins. In this case, each microspoiler array was subsequently activated and deactivated once per revolution.

Figures 20–23 present the results from four parametric trade studies investigating the control authority of the microspoiler mechanism where the data markers titled CFD/RBD Aero. refer to the aerodynamic data computed from the CFD/RBD virtual fly-out analysis and those titled Spark Range Aero. refer to aerodynamic data computed from the spark range test firing. For each study, the primary metric to evaluate control authority was the amount of cross-range (lateral) deflection of the projectile from its nominal or uncontrolled trajectory measured at the point of impact. The testbed projectile was the basic ANF with mass properties detailed in Table 1 and launch conditions intended to replicate that of a generic direct fire shot at Mach 3.0. The projectile rear stabilizing fins were also canted at approximately 0.5 deg to maintain spin rate. Approximate range for the intended target was just under 3.0 km. Nominal conditions for the

flight control system include a total included activation angle of 60 deg and an activation time of 1 s. Here, activation angle is defined as that portion of the projectile roll cycle where the microspoiler array is active (extended). Note that an activation angle of 0 deg corresponds to the nominal or uncontrolled trajectory in which the microspoiler mechanism is disabled. Activation time defines the amount of time following launch before the control system is engaged and the prototype maneuver is executed. Figure 20 shows the effective control authority with increasing number of active microspoiler arrays. In this case, the number of active microspoiler arrays was varied from one up to four separate quadrants, denoted MSC1–MSC4, respectively. The measured control authority was nearly linearly with increasing number of active microspoiler arrays up to a maximum cross-range deflection of approximately 47 m. Additionally, the maximum cross-range deflection using aerodynamic data estimated from both computational and experimental trajectories was quite similar with the CFD/RBD aerodynamic model predicting slightly higher maximum deflection.

**Fig. 20** Control authority vs number of MSCs.**Fig. 21** Control authority vs activation time.**Fig. 22** Control authority vs launch velocity.

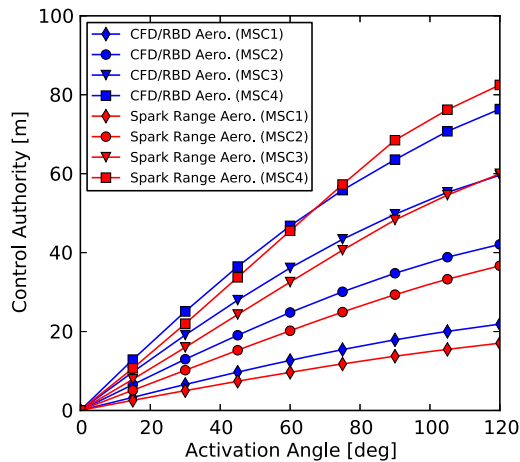


Fig. 23 Control authority vs activation angle.

The effects of varying both the activation time and launch velocity were also analyzed and are shown in Figs. 21 and 22. As expected, the effective control authority was significantly reduced with increasing activation time resulting from reduced maneuver time before impact. Also, the control authority was shown to increase with increasing launch velocity given the longer flight time and increased range associated with higher launch velocities. In both cases, the maximum control authority of the projectile using both the CFD/RBD and spark range aerodynamic data was very similar, with the largest discrepancy occurring at activation times of 2 s or longer and launch velocities below Mach 3.0.

Lastly, Fig. 23 shows the resulting control authority as the total included activation angle was increased from 0 to 120 deg. This trade study was quite significant in that, as the activation angle was increased, the resulting control authority increased from zero to just over 80 m for the case with four active microspoiler arrays (MSC4). Also note the measured deflection is again very similar between the CFD/RBD and spark range aerodynamic data with the CFD/RBD aerodynamic data predicting slightly higher deflection values when compared with the spark range data. However, the control authority predicted using the spark range aerodynamic model exceeds that of the CFD/RBD model for the case of four active microspoiler arrays (MSC4) and activation angles greater than 70 deg. This significant increase in control authority with increasing activation angle provides a key component to the active projectile control challenge in that during flight, the activation angle can be adjusted as needed to modulate the effective perturbation forces and moments such that the commanded trajectory is properly tracked. Although the active control capabilities of the ANF projectile are not included within this report, Dykes et al. [10] have shown that a dramatic reduction in impact dispersion is possible (on the order of 97%) using a simple proportional-integral-derivative guidance algorithm combined with the CFD/RBD aerodynamic data. When considering the similar level of control authority achieved using the spark range aerodynamic data, an equally dramatic reduction in impact dispersion is expected.

## VII. Conclusions

The work reported here details the aerodynamic characterization and resulting flight dynamic performance of a new control mechanism for supersonic finned projectiles. The mechanism incorporates a small array of protrusions, termed microspoilers, inserted between the rear stabilizing fins of the projectile, capable of producing a significant aerodynamic perturbation force from the shock wave interactions between the projectile body, rear stabilizing fins, and microspoilers. To characterize the aerodynamic effects of the microspoiler mechanism, trajectories for a basic finned projectile equipped with a single rigid microspoiler array were generated both computationally using a computational virtual fly-out analysis and experimentally from spark range test firing. In either case, the resulting aerodynamic models are largely in good agreement where

the major effect of the microspoiler array is the addition of trim forces and moments along with a small increase in axial forces. In contrast to the rigid microspoiler array used for aerodynamic characterization, the mechanism can be actively deployed or retracted in concert with the projectile roll angle to create significant control forces during flight. It was shown that the resulting control authority of a basic finned projectile equipped with such an active microspoiler control mechanism is quite large and capable of nearly 80 m cross-range deflection at just over 3.0 km range. Overall, the proposed microspoiler control mechanism continues to show great promise for active control of supersonic finned projectiles.

## References

- [1] Shoosmith, B., Birch, T., Mifsud, M., Meunier, M., and Shaw, S., "CFD Analysis of a Supersonic Projectile with Deflectable Nose Control," *Third Flow Control Conference*, AIAA Paper 2006-3200, June 2006. doi:10.2514/6.2006-3200
- [2] Costello, M., "Potential Field Artillery Projectile Improvement Using Movable Canards," Rept. ARL-TR-1344, U.S. Military Academy, West Point, NY, April 1997.
- [3] Rogers, J., and Costello, M., "Design of a Roll-Stabilized Mortar Projectile with Reciprocating Canards," *Journal of Guidance, Control, and Dynamics*, Vol. 33, No. 4, 2010, pp. 1026–1034. doi:10.2514/1.47820
- [4] Massey, K., McMichael, J., Warnock, T., and Hay, F., "Mechanical Actuators for Guidance of a Supersonic Projectile," *Journal of Spacecraft and Rockets*, Vol. 45, No. 4, 2008, pp. 802–812. doi:10.2514/1.31709
- [5] Massey, K., Guthrie, K., and Silton, S., "Optimized Guidance of a Supersonic Projectile Using Pin Based Actuators," *23rd Applied Aerodynamics Conference*, AIAA Paper 2005-4966, June 2005. doi:10.2514/6.2005-4966
- [6] Chandgadkar, S., Costello, M., Dano, B., Liburdy, J., and Pence, D., "Performance of a Smart Direct Fire Projectile Using a Ram Air Control Mechanism," *Journal of Dynamic Systems, Measurement and Control*, Vol. 124, No. 4, 2002, pp. 606–612. doi:10.1115/1.1514666
- [7] Corriveau, D., Berner, C., and Fleck, V., "Trajectory Correction Using Impulse Thrusters for Conventional Artillery Projectiles," *Proceedings of the 23rd International Symposium on Ballistics*, International Ballistics Soc., Tarragona, Spain, April 2007, pp. 639–646.
- [8] English, B., Gadiraju, P., Rinehard, C., Glezer, A., and Allen, M., "Gas Generator Actuator Arrays for Flight Control of Spinning Body Projectiles," *Proceedings of the 19th International Conference on Micro Electro Mechanical Systems*, IEEE Publications, Piscataway, NJ, Jan. 2006, pp. 806–809. doi:10.1109/MEMSYS.2006.1627922
- [9] Rogers, J., and Costello, M., "Control Authority of a Projectile Equipped with a Controllable Internal Translating Mass," *Journal of Guidance, Control, and Dynamics*, Vol. 31, No. 5, 2008, pp. 1323–1333. doi:10.2514/1.33961
- [10] Dykes, J., Montalvo, C., Costello, M., and Sahu, J., "Use of Microspoilers for Control of Finned Projectiles," *Journal of Spacecraft and Rockets*, Vol. 49, No. 6, 2012, pp. 1131–1140. doi:10.2514/1.A32274
- [11] Massey, K., and Silton, S., "Testing the Maneuvering Performance of a Mach 4 Projectile," *24th Applied Aerodynamics Conference*, AIAA Paper 2006-3649, June 2006. doi:10.2514/6.2006-3649
- [12] Bell, M., Watterson, J., and Lisk, D., "Numerical Study into a Local Protuberance Interaction with a Fin on a Supersonic Projectile," *47th Aerospace Sciences Meeting*, AIAA Paper 2009-1092, Jan. 2009. doi:10.2514/6.2009-1092
- [13] Sahu, J., "Time-Accurate Numerical Prediction of Free-Flight Aerodynamics of a Finned Projectile," *Journal of Spacecraft and Rockets*, Vol. 45, No. 5, 2008, pp. 946–954. doi:10.2514/1.34723
- [14] Costello, M., Gatto, S., and Sahu, J., "Using CFD/RBD Results to Generate Aerodynamic Models for Projectile Flight Simulation," *AIAA Atmospheric Flight Mechanics Conference and Exhibit*, AIAA Paper 2007-6582, Aug. 2007. doi:10.2514/6.2007-6582
- [15] Sahu, J., DeSpirito, J., Heavey, K., Costello, M., and Stahl, J., "Numerical Computations of Unsteady Aerodynamics of Maneuvering Projectiles," *DoD High Performance Computing Modernization Program Users Group Conference (HPCMP-UGC)*, IEEE Publica-

- tions, Piscataway, NJ, June 2009, pp. 88–95.  
doi:10.1109/HPCMP-UGC.2009.18
- [16] Sahu, J., and Heavey, K., “Parallel CFD Computations of Projectile Aerodynamics with a Flow Control Mechanism,” *Computers and Fluids Journal*, Vol. 88, No. 1, Dec. 2013, pp. 678–687.  
doi:10.1016/j.compfluid.2013.03.015
- [17] Goldberg, U., Peromian, O., and Chakravarthy, S., “Wall-Distance-Free k-Model with Enhanced Near-Wall Treatment,” *Journal of Fluids Engineering*, Vol. 120, No. 3, 1998, pp. 457–462.  
doi:10.1115/1.2820684
- [18] Bhagwandin, V., and Sahu, J., “Numerical Prediction of Dynamic Stability Derivatives for Finned Projectiles,” *Proceedings of the 27th International Symposium on Ballistics*, International Ballistics Soc., Freiburg, Germany, April 2013, pp. 186–197.
- [19] Sahu, J., “Numerical Computations of Dynamic Derivatives of a Finned Projectile Using a Time-Accurate CFD Method,” *AIAA Atmospheric Flight Mechanics Conference and Exhibit*, AIAA Paper 2007-6581, Aug. 2007.  
doi:10.2514/6.2007-6581
- [20] McCoy, R., *Modern Exterior Ballistics: The Launch and Flight Dynamics of Symmetric Projectiles*, Schiffer, Atglen, PA, 1999, pp. 187–214.
- [21] Carlucci, D., and Jacobson, S., *Ballistics: Theory and Design of Guns and Ammunition*, CRC Press, Boca Raton, FL, 2010, pp. 195–256.
- [22] Montalvo, C., and Costello, M., “Estimation of Projectile Aerodynamic Coefficients Using Coupled CFD/RBD Simulation Results,” *AIAA Atmospheric Flight Mechanics Conference*, AIAA Paper 2010-8249, Aug. 2010.  
doi:10.2514/6.2010-8249
- [23] Hainz, L., and Costello, M., “Modified Projectile Linear Theory for Rapid Trajectory Prediction,” *Journal of Guidance, Control, and Dynamics*, Vol. 28, No. 5, 2005, pp. 1006–1014.  
doi:10.2514/1.8027
- [24] Kaviratna, L., Costello, M., and Slegers, N., “Projectile Fire-Control Algorithm in a Spatially Varying Wind Field,” *Journal of Aerospace Information Systems*, Vol. 10, No. 11, 2013, 497–511.  
doi:10.2514/1.1010068.

M. Miller  
Associate Editor